Structure of the heterophilic interaction between the nectin-like 4 and nectin-like 1 molecules

Xiao Liu[a,b,1], Tai An[a,1], Dongdong Li[a], Zheng Fan[c], Pan Xiang[a], Chen Li[a], Wenyi Ju[a], Jianing Li[a], Gen Hu[a], Bo Qin[d], Bin Yin[a], Justyna Aleksandra Wojdyla[e], Meitian Wang[e], Jiangang Yuan[a], Boqin Qiang[a], Pengcheng Shu[a,2], Sheng Cui[d,2], and Xiaozhong Peng[a,b,2]

[a]The State Key Laboratory of Medical Molecular Biology, Neuroscience Center, Medical Primates Research Center and Department of Molecular Biology and Biochemistry, Institute of Basic Medical Sciences, Chinese Academy of Medical Sciences, School of Basic Medicine, Peking Union Medical College, 100005 Beijing, China; [b]Institute of Medical Biology, Chinese Academy of Medical Sciences, Peking Union Medical College, 650118 Kunming, China; [c]Core Facility, Institute of Microbiology, Chinese Academy of Sciences, 100101 Beijing, China; [d]Ministry of Health Key Laboratory of Systems Biology of Pathogens, Institute of Pathogen Biology, Chinese Academy of Medical Sciences and Peking Union Medical College, 100730 Beijing, China; and [e]Macromolecular Crystallography, Swiss Light Source at the Paul Scherrer Institute, CH-5232 Villigen, Switzerland

Edited by Johann Deisenhofer, The University of Texas Southwestern Medical Center, Dallas, TX, and approved December 14, 2018 (received for review June 26, 2018)

Nectin-like (Necl) molecules are Ca^{2+}-independent Ig-like transmembrane cell adhesion molecules that participate in junctions between different cell types. The specific cell–cell adhesions mediated by Necl proteins are important in neural development and have been implicated in neurodegenerative diseases. Here, we present the crystal structure of the mouse Necl-4 full ectodomain and the structure of the heterophilic Necl ectodomain complex formed by the mNecl-4 and mNecl-1 ectodomains. We demonstrate that, while the ectodomain of mNecl-4 is monomeric, it forms a stable heterodimer with Ig1 of mNecl-1, with an affinity significantly higher than that observed for self-dimerization of the mNecl-1 ectodomain. We validated our structural characterizations by performing a surface plasmon resonance assay and an Fc fusion protein binding assay in mouse primary dorsal root ganglia neurites and Schwann cells and identified a selection of residues important for heterophilic interactions. Finally, we proposed a model of Necl binding specificity that involves an induced-fit conformational change at the dimerization interface.

crystal structure | ectodomain | heterophilic interaction | nectin-like | cell adhesion

Ig-like cell adhesion molecules (IgCAMs), which comprise one of the largest groups of cell adhesion molecules, can mediate *trans* molecular interactions in cell–cell contacts and form *cis* interactions within the same membrane. The precise assembly of these interaction networks depends on the homophilic or heterophilic binding selections of the adhesion molecules through their extracellular domains (1). These molecules play essential roles in various cellular processes, particularly the development of the nervous system (2). However, the mechanism responsible for this selection remains to be clarified through the structural characterization of the IgCAM domains involved in homophilic and heterophilic binding.

Nectin and nectin-like (Necl, also known as CADM or SynCAM) molecules are Ca^{2+}-independent IgCAMs (3, 4). Nectins constitute a family comprised of four members (i.e., Nectin-1, -2, -3, and -4) (5) while the Necl family contains five members (i.e., Necl-1 through Necl-5) (6). All members of these families contain an extracellular region with three Ig-like domains, a single transmembrane region, and a short cytoplasmic region. Nectins and Necls are classified based on their ability to bind afadin. Nectins have a conserved motif of four amino acid residues (Glu/Ala-X-Tyr-Val) in their carboxyl terminal region and can bind the PDZ domain of afadin, whereas Necl proteins lack this activity (6, 7). Although nectins and Necl proteins share similar names based on the folding of their ectodomains, a recent bioinformatics study found that these molecules could be clearly segregated into nectin and Necl subgroups (8). Although Necl-5 (also known as poliovirus receptor) is unable to bind afadin, it is more closely related to nectins at the sequence level (3, 8, 9).

Similar to nectins, molecules in the Necl family mediate cell adhesion through homophilic or heterophilic interactions. All Necl proteins are localized to cellular plasma membranes, and most Necls can form *cis*-dimers on the surface of the same cell (6, 9–11) or mediate opposing cell adhesion by *homo-* or *hetero-trans*dimerization via the interaction of Ig-like domains (4). For example, Necl-1 can form homophilic interactions with itself and heterophilic interactions with other Necl family members and members of the nectin family *in trans* (9, 10, 12) whereas Necl-2 interacts with Necl-1, -2, and -3 homophilically and heterophilically (12, 13). Notably, Necl-4 is found to form only heterophilic interactions with Necl-1 *in trans* (14, 15), and whether Necl-4 forms homophilic interactions is currently controversial (16, 17). Recent structural studies have proposed several mechanisms for homophilic interactions (18–22), as well as interactions between nectin/Necl and other families of IgCAM cell adhesion

Significance

Cell–cell adhesion is fundamental for the development of multicellular organisms. Dysfunctional cell adhesion leads to severe developmental defects and inherited diseases. The Necl proteins belong to a subfamily of immunoglobulin cell adhesion molecules. Although numerous structural characterizations of the homophilic interactions of Necl proteins are available, the structural basis of heterophilic Necl interactions has remained unclear for decades. Here, we determined the structure of a Necl heterodimer comprising the ectodomains of mouse Necl4 and Necl1, providing groundbreaking structural insights into Necl heterodimerization. We show that Necl4 and Necl1 heterophilic interaction is significantly stronger than Necl1 homodimeric interaction. Based on our findings, we proposed an induced-fit mechanism for the binding specificity and heterophilic interaction of Necl proteins.

Author contributions: J.Y., B. Qiang, P.S., S.C., and X.P. designed research; X.L., T.A., D.L., Z.F., P.X., C.L., W.J., J.L., G.H., B. Qin, B.Y., J.A.W., and M.W. performed research; X.L., T.A., D.L., Z.F., J.A.W., M.W., S.C., and X.P. analyzed data; and X.L., T.A., P.S., S.C., and X.P. wrote the paper.

The authors declare no conflict of interest.

This article is a PNAS Direct Submission.

Data deposition: Coordinates and structure factors for the X-ray structures of the mNecl-4 and the mNecl-4–mNecl-1 ectodomain complex have been deposited in the Protein Data Bank, www.wwpdb.org (PDB ID codes 5ZO1 and 5ZO2, respectively).

[1]X.L. and T.A. contributed equally to this work.

[2]To whom correspondence may be addressed. Email: pengcheng_shu@ibms.pumc.edu.cn, cui.sheng@ipb.pumc.edu.cn, or pengxiaozhong@pumc.edu.cn.

This article contains supporting information online at www.pnas.org/lookup/suppl/doi:10.1073/pnas.1810969116/-/DCSupplemental.

Published online January 23, 2019.

molecules (23–25) or virus-encoded proteins (26–29). Remarkably, the structure of TIGIT complexed with nectin-2 offers atomic-level insight into the heterophilic interaction between Ig-like domains. By contrast, the structure of heterophilic interactions within the Necl family remains unknown. Hence, the full ectodomain structure of the Necl family and the structures of heterophilic interactions among different Necl family members remain to be identified.

Heterophilic interactions among Necl proteins contribute to multiple developmental processes, including synapse formation (30, 31), axon guidance (13), myelination (14, 32), and pathological diseases, such as Alzheimer's disease (33), autism spectrum disorder (ASD) (34–36), attention-deficit hyperactivity disorder (ADHD) (37, 38), and cancer (39–41). Among the heterophilic interactions among Necl family members, the *trans* interaction between Necl-4 and Necl-1 is critical for their functions (14, 15). Heterophilic binding between axonal Necl-1 and glial Necl-4 mediates axon–Schwann cell interactions during myelination (14, 15, 32). Additionally, the disruption of Necl-1 results in a developmental delay in axonal myelination in the optic nerve and spinal cord in Necl-1–deficient mice (32). Furthermore, Necl-4–deficient mice develop focal hypermyelination, abnormal axon-glial contact, and redistribution of ion channels along the axon (42). Hence, understanding the roles and mechanisms of IgCAMs in multicellular organisms by revealing how Necl-1 interacts with Necl-4 is highly important.

To elucidate the molecular and structural basis of the adhesion of neuronal cells and to understand the specificity of different Necls, we have determined the crystal structures of the full ectodomain of Necl-4 alone and the Necl-4/Necl-1 ectodomain complex using X-ray crystallographic approaches, including a cutting-edge native single-wavelength anomalous diffraction (SAD) phasing technique. Our structural characterization shows that, while the ectodomain of Necl-4 alone is monomeric, it forms a heterodimer with Necl-1 via their Ig1 domains, and we observed significant conformational changes in the F-and G-loop of the Ig1 domain of Necl-4. Furthermore, combining functional and mutagenesis analyses, we identified a collection of residues at the interface regions between Necl-4 and Necl-1 that are critical for the heterophilic interaction between the two molecules. Finally, we proposed a model of Necl binding specificity that involves an induced-fit conformational change at the dimerization interface.

Results

The Full Ectodomain of Mouse Necl-4 Exists as a Monomer in Solution but Forms a Heterophilic Dimer with Necl-1 via Their Ig1 Domains. The WT full ectodomain (Ig1 to Ig3) of mouse Necl-4 (mNecl-4) was overexpressed in High Five cells and purified. The molecular mass of the recombinant mNecl-4 full ectodomain (0.6 mg/mL) measured by sedimentation velocity analytical ultracentrifugation (svAUC) was ∼36.349 kDa (*SI Appendix*, Fig. S1*A*), which is approximately equal to the theoretical molecular mass of mNecl-4 with four N-linked glycans purified from High Five cells (∼38.216 kDa). The results indicate that the full ectodomain of mNecl-4 exists as a monomer in solution, which is consistent with previous reports that Necl-4 cannot form homodimers (14, 43). The Ig1 domain of mouse Necl-1 (mNecl-1) (calculated molecular mass of ∼15.982 kDa) was overexpressed in *Escherichia coli* cells and purified. The molecular mass of the Ig1 domain of mNecl-1 (0.7 mg/mL) measured by svAUC was ∼28.843 kDa (*SI Appendix*, Fig. S1*B*), which was nearly double the theoretical molecular mass, indicating that the Ig1 domain of mNecl-1 is dimeric in solution.

To investigate the heterophilic interaction between the ectodomains of mNecl-1 and mNecl-4, we performed a His tag pulldown assay with the purified proteins. Untagged mNecl-1 Ig1 was not detected in the flow-through fraction; instead, it was coeluted with mNecl-4-ECD-His_6 (*SI Appendix*, Fig. S1*C*). Together, the His tag pulldown assay demonstrated that the ectodomain of mNecl-4 forms a heterophilic dimer with the Ig1 domain of mNecl-1, which is consistent with the observations reported in previous studies (14, 15, 43).

Crystallization of the mNecl-4 and mNecl-1 Ectodomain Complex. To reveal the structural basis of the heterophilic interaction between the mNecl-4 and mNecl-1 ectodomains, we carried out crystallographic studies. First, we expressed the full ectodomain (Ig1 to Ig3) of mNecl-4 in High Five cells and the Ig1 domain of mNecl-1 in *E. coli* cells. Then, we mixed the purified proteins at a 1:1 molar ratio and incubated the mixture on ice to allow the formation of the protein complex. The complex was finally purified by size-exclusion chromatography before the crystallization trials. Unfortunately, neither the crystals of the mNecl-4 and mNecl-1 ectodomain complex nor the crystals of the mNecl-4 ectodomain diffracted X-rays to high resolution (∼10 Å). In the SDS/PAGE analysis of the protein samples, we found that the recombinantly produced mNecl-4 ectodomain exhibited a heterogeneous molecular mass (*SI Appendix*, Fig. S1 *D* and *E*). The heterogeneity of the mNecl-4 ectodomain was probably due to glycosylation. Therefore, we predicted the glycosylation sites of mNecl-4 using the NetNGlyc server (www.cbs.dtu.dk/services/NetNGlyc/) and predicted that four residues (i.e., N31, N67, N262, and N286) are potential glycosylation sites. Subsequently, we introduced Asn-to-Gln mutations at these potential glycosylation sites. While mutations N31Q, N262Q, and N286Q could significantly improve the homogeneity of the recombinant protein (*SI Appendix*, Fig. S1 *D* and *E*), mutation N67Q led to the insolubility of the protein, suggesting that glycosylation at residue N67 is essential for protein folding.

To assess whether mNecl-4 ectodomains bearing these glycosylation site mutations maintain a structure similar to that of the WT protein, we carried out circular dichroism (CD) spectrometry (*SI Appendix*, Fig. S2). As shown in *SI Appendix*, Fig. S2, the CD profile of the WT mNecl-4 ectodomain had the typical characteristics of β-sheet–rich domains. This finding is consistent with the prediction that Necl-4 contains Ig-like β-sheet–rich domains. The CD profile of the mNecl-4 ectodomain bearing the N31Q, N262Q, and N286Q mutations overlaid well with the CD profile of the WT mNecl-4 ectodomain, confirming that these glycosylation site mutations did not alter the overall folding. Therefore, we used the ectodomain of mNecl-4 containing the N31Q, N262Q, and N286Q mutations for further structural characterization.

Structure Determination. Consistent with the improved homogeneity of mNecl-4 with the N31Q, N262Q, and N286Q mutations, the crystals of this mutant diffracted X-rays to 2.2 Å. However, extensive molecular replacement trials with all known structures of Ig superfamily molecules as the searching model were unsuccessful in solving the crystal structure of the mNecl-4 full ectodomain. Therefore, we employed an experimental phasing technique termed native SAD phasing (44, 45) to solve this structure. We took advantage of the conserved disulfide bridge present in all Ig domains (Ig1 to Ig3) of mNecl-4, which together provide six native sulfur atoms that contribute to anomalous signals. We used an X-ray with a wavelength of 2.077 Å and collected 16 datasets from a single crystal at two separate positions and at different orientations [chi angles (46) ranging from 0° to 35°]. The final dataset was prepared by scaling and merging the 14 datasets; thus, the anomalous signal extended to 3.2 Å. Then, an interpretable electron density map was calculated using SHELXC/D/E, which enabled the initial model building. We located 288 of the 293 amino acids of the mNecl-4 ectodomain and identified residue N67, which contains N-linked glycans. To improve the overall data quality, we collected a 2.2-Å native dataset using X-ray diffraction at a wavelength of 1.000 Å. The final structure of the mNecl-4 ectodomain was solved by molecular replacement using the initial model as the searching model.

Using our de novo crystal structure of mNecl-4 and the previously determined crystal structure of the human Necl-1 Ig1 domain (PDB ID code 1Z9M) as the searching models, we finally solved the crystal structure of the mNecl-4 and mNecl-1 ectodomain complex by molecular replacement. Two mNecl-4 molecules and one mNecl-1 Ig1 domain were present in the asymmetric unit (ASU). The Ig1 domain of mNecl-1 interacts through its Ig1 domain with only one of the mNecl-4 molecules present in the ASU. The data collection, refinement parameter statistics, and structure validation reports of the crystal structures of the mNecl-4 ectodomain and the mNecl-4 and mNecl-1 ectodomain complex are summarized in Table 1.

Crystal Structure of the mNecl-4 Full Ectodomain. The final refined structure of the mNecl-4 full ectodomain contains residues 29 to 316. The extreme N-terminal signal sequence (residues 1 to 24) was removed for insertion into a baculovirus expression vector. Residues 25 to 28 were excluded from the final model due to the lack of electron density in this region. The full ectodomain of mNecl-4 contains three tandem Ig superfamily domains (IgSFs) (Figs. 1*A* and 2).

To our knowledge, the available crystal structures of nectin and Necl family members reveal homodimeric assemblies (18–22), except for Necl-4. Using PISAePDB software, we did not detect any oligomeric assembly in the crystal structure, suggesting that the mNecl-4 ectodomain is monomeric, which is consistent with our biochemical results. The N-terminal domain (Ig1) spans residues 29 to 122. Similar to other Ig variable-like domains, Ig1 contains two layers of β-sheets, comprising β-strands ABED and CC′C″FG (Figs. 1*A* and 2). A disulfide bridge is formed between C104 of the F strand from the front layer and C44 of the B strand from the back layer. Residue N67, whose mutation leads to the insolubility of the mNecl-4 ectodomain, contains N-linked carbohydrates. The final electron density map shows that the asparagine side chain is linked to two *N*-acetylglucosamine molecules (β 1–4-linked GlcNAc2) bearing an α 1–6 fucosylation on the first GlcNAc. The N67-linked carbohydrate moiety acts as a lid covering the hydrophobic pocket formed by the loop between strands D and

Table 1. Data collection and refinement statistics

Parameters	mNecl-4 full ectodomain (Ig1 to Ig3) native SAD dataset	mNecl-4 full ectodomain (Ig1 to Ig3) high-energy dataset (PDB ID code 5ZO1)	mNecl-4 full ectodomain complexed with mNecl-1 Ig1 domain (PDB ID code 5ZO2)
Data collection			
Space group	I4122	I4122	P321
Cell dimensions			
a, b, c, Å	109.09, 109.09, 181.50	109.22, 109.22, 182.10	207.68, 207.68, 53.01
α, β, γ (°)	90.00, 90.00, 90.00	90.00, 90.00, 90.00	90.00, 90.00, 120.00
X-ray source	SLS BEAMLINE X06DA	SLS BEAMLINE X06DA	SSRF BEAMLINE BL17U
Wavelength, Å	2.077 (sulfur phasing)	1.000	0.97776
Data range, Å	47.11 to 2.14 (significant anomalous correlation to 3.2 Å)	47.30 to 2.20	49.84 to 3.30
Reflections unique	54,616*	53,627*	19,407
R_{sym}[†] (last shell)	0.13 (2.22)	0.14 (0.94)	0.22 (1.07)
$I/\sigma I$	48.25 (0.92)	12.15 (2.02)	6.96 (1.64)
Completeness, % (last shell)	0.95 (0.71)	0.99 (0.98)	0.97 (0.98)
Redundancy (last shell)	132.86 (8.31)	6.98 (6.78)	5.68 (5.80)
Refinement			
Resolution range, Å	\	47.30–2.20	49.84–3.30
Reflections, cutoff, % reflections in cross-validation	\	28,426, >1.35, 4.88	19,399, >1.34, 5.17
R_{work}[‡]/R_{free}[§] (last shell)	\	0.199/0.220 (0.252/0.295)	0.243/0.302 (0.305/0.381)
Atoms			
Nonhydrogen protein atoms	\	2,510	4,591
Protein	\	2,273	4,553
Solvent	\	200	0
B-factors average, Å^2	\	48.64	65.70
Protein, Å^2	\	47.32	65.45
Solvent, Å^2	\	43.30	0
rmsd			
Bond lengths, Å	\	1.783	1.621
Bond angles (°)	\	0.008	0.011
Validation			
MolProbity score	\	1.68, 96th percentile[¶]	2.36, 99th percentile[¶]
Clashscore, all atoms	\	8.47, 93rd percentile[¶]	13.63, 97th percentile[¶]
% Poor rotamers		0	1.62
% residues in favored regions, allowed regions, outliers in Ramachandran plot		96.85, 3.15, 0	89.71, 9.43, 0.86

\, data not applicable.
*Friedel pairs are treated as different reflections.
[†]$R_{sym} = \sum_{hkl}\sum_j |I_{hkl,j} - I_{hkl}|/\sum_{hkl}\sum_j I_{hkl,j}$, where I_{hkl} is the average of the symmetry-related observations of a unique reflection.
[‡]$R_{work} = \sum_{hkl} ||F_{obs}(hkl)|-|F_{calc}(hkl)||/\sum_{hkl}|F_{obs}(hkl)|$.
[§]R_{free} = the cross-validation *R* factor for 5% of reflections against which the model was not refined.
[¶]The 100th percentile is the best among structures of comparable resolution; the 0th percentile is the worst. For clashscore, the comparative set of structures was selected in 2004 for the MolProbity score in 2006.

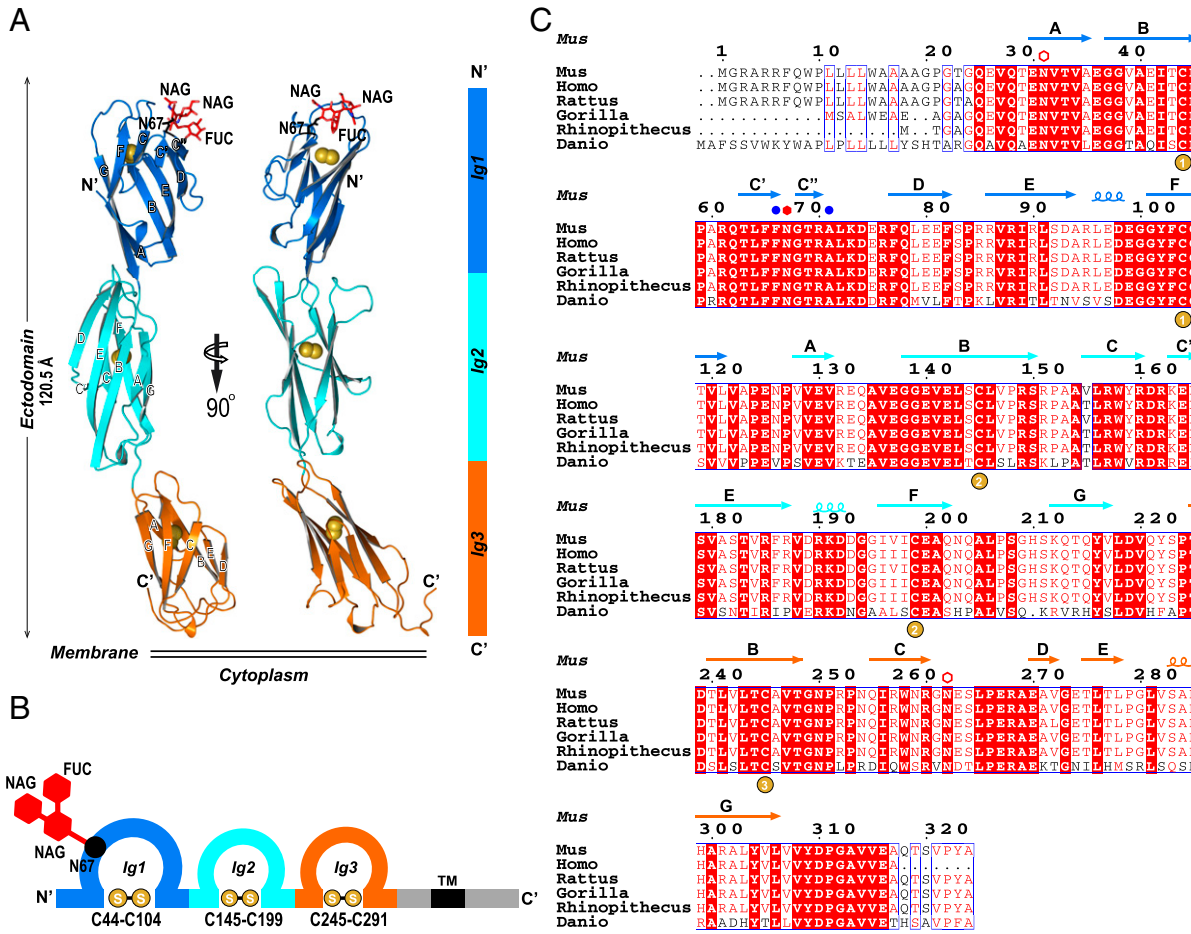

Fig. 1. (*A*) Ribbon model of the mNecl-4 ectodomain. Ig1 is shown in blue, Ig2 is shown in cyan, and Ig3 is shown in orange. The conserved disulfide bridge of each IgSF domain is shown in golden spheres. The length of the ectodomain is indicated. (*B*) Schematic diagram of the domain organization of mNecl-4 using the same color scheme used in *A*. (*C*) Structure-based multiple sequence alignment of Necl-4 from different organisms. The secondary structural elements are aligned to the top of the sequence using the same color scheme used in *A*. Residues with glycosylation are marked with filled hexagons, and residues that were predicted as glycosylation sites and mutated to asparagine are marked with open hexagons. Conserved cysteines that form S–S bridges are marked with golden spheres. The blue circle represents the key amino acid residues for heterophilic binding of the mNecl-4 ectodomain to mNecl-1 Ig1.

E and the loop between strands B and C, which involves residues Y49, I53, S52, F82, and P84. Therefore, glycans may play a critical role in stabilizing the overall folding of the mNecl-4 ectodomain by protecting the hydrophobic patch on the surface of Ig1, which is consistent with our biochemical results. Domains Ig2 and Ig3 of mNecl-4 also adopt an IgSF fold (Fig. 1*A*). The Ig2 domain spans residues 123 to 222 and contains eight β-strands in two layers connected by a disulfide bridge between residues C145 and C199. The Ig3 domain spans residues 223 to 336 and contains seven β-strands in two layers connected by a disulfide bridge between residues C245 and C291.

We compared the structures of the full ectodomain of mNecl-4 and each individual IgSF domain with known protein structures obtained from a public database using the Dali server (ekhidna.biocenter.helsinki.fi/dali_server). The best hit for the entire ectodomain of mNecl-4 was the human nectin-1 ectodomain (Ig1 to Ig3) (PDB ID code 4FMF). The Dali Z score was 19.6, the rmsd value was 4.0 Å, and 271 positions were aligned. The best hit for the mNecl-4 Ig1 domain was the human Necl-2 ectodomain Ig1 domain (PDB ID code 4H5S). The Dali Z score was 15.6, the rmsd value was 1.3 Å, and 91 positions were aligned. The best hit for the mNecl-4 Ig2 domain was the Ig2 domain of human signal regulatory protein (SIRP) alpha (PDB ID code 2WNG). The Dali Z score was 13.6, the rmsd value was 1.7 Å, and 98 positions were aligned. The best hit for the mNecl-4 Ig3 domain was the human Necl-2 ectodomain Ig1 domain (PDB ID code 4MYW). The Dali Z score was 13.7, the rmsd value was 1.6 Å, and 87 positions were aligned. Thus, our structural analysis shows that three Ig domains of mNecl-4 share similar folding with other nectin/Necl ectodomains.

Crystal Structure of the mNecl-4/mNecl-1 Ectodomain Complex. In the final structure of the mNecl-4 and mNecl-1 ectodomain complex, we found two molecules of the mNecl-4 ectodomain and one molecule of the mNecl-1 Ig1 domain (Fig. 3*A*). The Ig1 domain of one mNecl-4 ectodomain (chain C) interacts with mNecl-1 whereas the electron-density of the Ig1 domain of the other mNecl-4 ectodomain (chain A) was essentially missing, indicating that this domain is highly flexible, likely due to the lack of contacts with other molecules in the crystal.

The binding mode between mNecl-4 Ig1 and mNecl-1 Ig1 is similar to that observed for the homodimerization of mNecl-1 Ig1 (PDB ID code 1Z9M) (22). The heterodimer of mNecl-4 Ig1 and mNecl-1 Ig1 has an overall twofold symmetry. A structural comparison of mNecl-4 Ig1 and mNecl-1 Ig1 aligned 93 residues with an rmsd value of 1.2 Å even though the sequence identity of the Ig1 domains was only 35.5%. The C strands of mNecl-4 Ig1 and mNecl-1 Ig1 are in close proximity and form the center of the heterodimer. Using PDBePISA, we calculated that the interfacial area between the heterodimer of mNecl-4 Ig1 and mNecl-1 Ig1 was 764.3 Å^2, which was larger

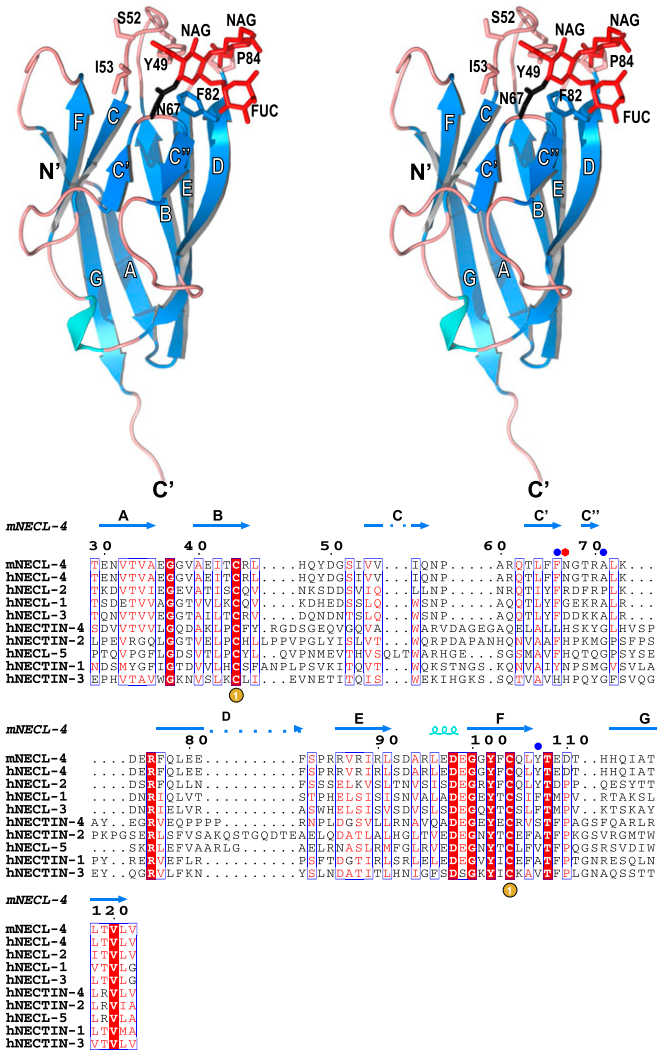

Fig. 2. Structure of the mNecl-4 Ig1 domain. (*Upper*) Wall-eye stereo plot of mNecl-4 Ig1 with secondary structural elements colored as follows: α- helix in cyan, β-sheet in blue, and loop in brown. Glycans linked to N67 (black) are shown as a stick model. The carbohydrate moieties cover a hydrophobic pocket formed by the loop between strands D and E and the loop between strands B and C. Residues forming the hydrophobic pocket are shown as a stick model. (*Lower*) Structure-based multiple sequence alignment of human nectin and nectin-like molecules.

than that for the mNecl-1 Ig1 homodimer (708.8 Å^2), suggesting that the heterophilic binding of the mNecl-4 and mNecl-1 ectodomains is stronger than the homophilic binding of Necl-1. The interaction interface between mNecl-4 Ig1 and mNecl-1 Ig1 includes a cluster of polar and hydrophobic contacts that involve residues from the front layers of the Ig1 domains (Fig. 3*B*). The predominant hydrophobic contacts include antiparallel aromatic ring stacking between F66 of mNecl-4 and F70 of mNecl-1; in addition, Y107 of mNecl-4 accommodates a hydrophobic patch formed by T67, A75, and L76 of mNecl-1. The principal polar contacts between mNecl-4 Ig1 and mNecl-1 Ig1 include a hydrogen bond between the side chains of H113 and Q66 and a hydrogen bond between the side chain OH group of Y107 of mNecl-4 and the backbone NH group of T67 of mNecl-1. A detailed list of the contacts between mNecl-4 Ig1 and mNecl-1 Ig1 is provided in Table 2.

Key Residues at the Binding Interface of the mNecl4–mNecl1 Complex. We next performed surface plasmon resonance (SPR) binding assays to assess the importance of structurally defined contact residues in heterocomplex formation. We detected heterophilic binding between WT Necl-4 (Necl-4 WT) and Necl-1 (Necl-1 WT), with K_D values of ∼1.1 μM (Fig. 4*A*). Then, a series of residues at the contact sites were substituted by alanine, except for Ala75 of mNecl-1 and Ala71 of mNecl-4, which were substituted by phenylalanine, either individually or together. A detailed list of the mutated residues of mNecl-4 and mNecl-1 is shown in Table 3. Our SPR results clearly showed that individual mutations of amino acids F70A, A75F, and F111A of mNecl-1 abolished the heterophilic interaction with mNecl-4 WT, with K_D values of ∼98.3 μM, 111 μM, and 169 μM, respectively (Fig. 4 *B*–*D*). The double F70A and F111A mutant of mNecl-1 had no response to mNecl-4 WT (*SI Appendix*, Fig. S3*A*). Individual F66A, A71F, and Y107A mutants of mNecl-4 failed to heterophilically interact with mNecl-1 WT, with K_D values over 350 μM (Fig. 4 *E*–*G*). The same results were obtained for the interaction of the F66A Y107A double mutant of mNecl-4 with mNecl-1 WT (*SI Appendix*, Fig. S3*K*). Other mutants exhibited relatively stronger heterophilic binding, with K_D values from 2.44 μM to 66.5 μM (Table 3 and *SI Appendix*, Fig. S3).

We further verified whether the structurally observed key residues at the heterophilic interface mediated *trans* interactions under physiological conditions. Previous studies have shown that Necl-4 and Necl-1 mediate critical interactions between Schwann cells and axons during myelination (14, 15). To determine whether these key residues affect heterophilic binding at the cellular level, we performed an Fc fusion protein binding experiment in primary cultured dorsal root ganglion (DRG) neurites or Schwann cells, as previously described (14, 15, 47, 48). With anti-human Fc-Cy3, the soluble WT Necl-4-Fc fusion protein robustly labeled axons (Fig. 5*C*), but not axons derived from Necl-1–null mice (Fig. 5*H*). The

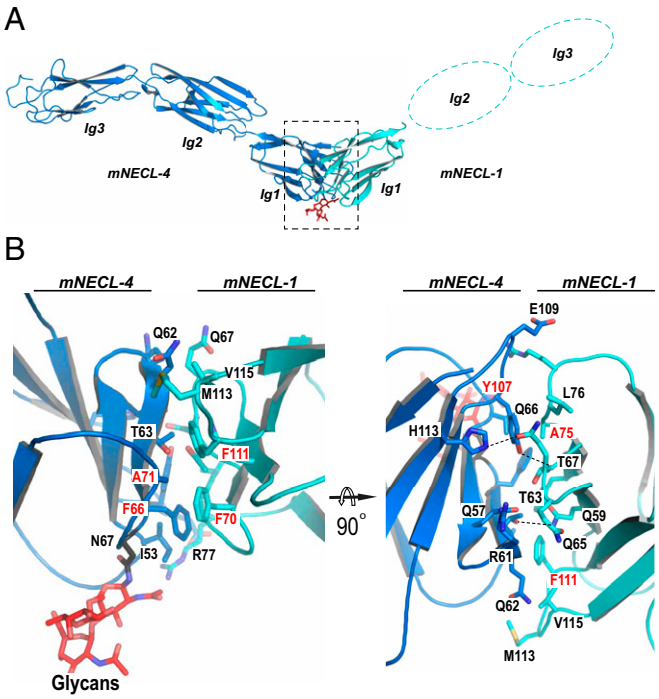

Fig. 3. Structure of the mNecl-4 and mNecl-1 ectodomain complex. (*A*) Ribbon model of the mNecl-4 and mNecl-1 ectodomain complex structure; mNecl-4 is shown in blue, and mNecl-1 is shown in cyan. Ig2 and Ig3 of mNecl- 1 are superimposed using dashed lines in cyan. (*B*) Close-up views of the interfacial contacts between mNecl-4 Ig1 and mNecl-1 Ig1. Residues involving interactions between mNecl-4 and mNecl-1 are shown as a stick model. Polar contacts are indicated by dashed lines. Glycans are shown as a stick model and colored in red.

Table 2. Predominant residues involved in the interaction between mNecl-4 and mNecl-1 Ig1

Atom from mNecl-4	Atom from mNecl-1 Ig1
Predominant hydrophobic contacts at the interface	
Phe-66	Phe-70
Tyr-107	Thr-67
Tyr-107	Ala-75
Tyr-107	Leu-76
Direct hydrogen bonds	
His-113	Glu-66
Tyr-107-OH	Thr-67-NH

Necl-1-Fc fusion protein bound to Schwann cells (Fig. 5*K*) but failed to bind to Schwann cells derived from Necl-4–null mice (Fig. 5*P*). These results were consistent with previous reports and with the idea that Necl-4 on Schwann cells binds heterophilically to Necl-1 on axons. We next examined whether the mutants of Necl-1-Fc and Necl-4-Fc could bind to their partners on primary cultured cells. As expected, all of the single or combined mutants of key residues found in the SPR assay showed reduced binding to the cells (Fig. 5 *D*–*F*, and *L*–*N* and *SI Appendix*, Fig. S4 *A*, *B*, *E*, and *F*), which indicated that the substitution of key residues abrogated the *trans* interaction between Schwann cells expressing Necl-4 and axonal Necl-1. To exclude false-positive binding in this experiment, we introduced an R45A mutant of mNecl-4 and an E36A mutant of mNecl-1, which depart from the binding surface based on the structure; these mutants could strongly bind to neurites (Fig. 5*B*) or Schwann cells (Fig. 5*J*), as expected. On the other hand, the Q62A mutant and N31Q N262Q N286Q triple mutant of the mNecl-4-Fc protein, the Q59A and V115A mutants of the mNecl-1-Fc protein, which showed slight changes in SPR assays compared with the WT, exhibited weak binding to neurites (*SI Appendix*, Fig. S4 *C* and *D*) and Schwann cells (*SI Appendix*, Fig. S4 *G* and *H*). Thus, mutational and functional analyses strongly support the identification of key residues responsible for the heterophilic interaction at the dimer interface.

Discussion

Comparison Between Monomer, Homophilic Interaction, and Heterophilic Interaction. Previous reports have shown that the CC′C″FG β-sheets of two identical nectin Ig1 domains participate in the formation of the homophilic interactions (18–20). Notably, a conserved aromatic residue in the loop between the F and G β-strands is crucial for the formation of the hydrophobic pocket by the C′ and C″ strands of the partner molecule (19). Our structural and mutagenesis characterizations demonstrated that the loop between the F and G β-strands (designated the F-and-G-loop) of the Ig1 domain of mNecl-4 or mNecl-1 was directly involved in the heterophilic interaction. The crystal structure of the mNecl-4 and mNecl-1 complex shows that the mode of interaction between the heterophilic Ig1 domains closely resembles the homophilic interaction between the human Necl-1 (hNecl-1) Ig1 domains (Fig. 3*B* and PDB ID code 1Z9M) (22). Because of the high conservation between the Ig1 domains of human and mouse Necl-1 (22), we superimposed the structure of the bound Ig1 domain of mNecl-4 from PDB ID code 5ZO2 with the structure of Ig1 of hNecl-1 from PDB ID code 1Z9M and showed that their F-and-G-loops adopted nearly identical conformations (*SI Appendix*, Fig. S5*A*); in addition, residues Y107 and T111 from the F-and-G-loop of mNecl-4 exhibited side chain conformations similar to those of their structural counterparts, F111 and V115, in mNecl-1. Hence, we designated this conformation the "dimerization-permissive conformation." In contrast, the crystal structure of the mNecl-4 ectodomain suggests that it does not form homophilic dimers in the crystal, which is consistent with our biophysical characterizations showing that the mNecl-4 ectodomain is monomeric. By comparing the structures of the bound (PDB ID code 5ZO2) and unbound (PDB ID code 5ZO1) Ig1 domain of mNecl-4, we observed a large conformational rearrangement of the F-and-G-loop. In particular, the tip of the loop significantly shifts away from the Ig1 domain (*SI Appendix*, Fig. S5*B*) in unbound mNecl-4. This unusual conformation of the F-and-G-loop clearly altered the structure of the dimerization interface; thus, this confirmation may impair the self-dimerization of the mNecl-4 ectodomain due to steric hindrance. This conformational change accounted for the largest structural deviation between the bound and unbound Ig1 domains of mNecl-4, including not only flipping of the side chains but also a large displacement of the backbone trace (*SI Appendix*, Fig. S5*C*). Therefore, we designated this conformation a "dimerization-nonpermissive conformation." We hypothesize that, in the absence of mNecl-1, the F-and-G-loop of the mNecl-4 ectodomain adopts a dimerization-nonpermissive conformation that prevents homophilic interactions between monomers. In the presence of mNecl-1, the Ig1 domain of mNecl-1 might induce a conformational switch in the F-and-G-loop of mNecl-4 from dimerization nonpermissive to dimerization permissive, allowing for heterophilic interactions.

To understand the mechanism by which the F-and-G-loop of mNecl-4 switches between two distinct conformations and facilitates heterophilic dimerization, we first performed multiple sequence alignment analyses (Fig. 2). We found that a conserved proline residue on the F-and-G-loop is invariant in all other nectins and Necls, but, in Necl-4 proteins, this proline is replaced by an aspartic acid, which appears to correlate with the unique stoichiometry of Necl-4. Due to its distinctive side chain structure, proline has a pronounced conformational rigidity that is greater than that of all other amino acids. Therefore, the presence of a proline in the F-and-G-loop could serve to fix its conformation to the dimerization-permissive conformation, as observed in previously reported homophilic interactions. In contrast, the structural counterpart of this proline in mNecl-4 is an aspartic acid, which allows for more flexibility; thus, aspartic acid may allow the dimerization-nonpermissive conformation of the F-and-G-loop, as observed in the crystal structure of the unbound mNecl-4 ectodomain. The switch from the dimerization-nonpermissive conformation to the permissive conformation may occur only in the presence of other Necl proteins, such as mNecl-1 in this case, which have already adopted the dimerization-permissive conformation to allow the switch from the monomer to the homophilic dimer. In structural and biophysical experiments, we demonstrated that the interaction between mNecl-1 and mNecl-4 is significantly stronger than the homodimerization of mNecl-1; therefore, in the presence of mNecl-1, the equilibrium is shifted toward the formation of heterophilic dimers. By combining the available structural and biophysical results, we present a model of the changes that occur among the monomeric conformation, homophilic interactions, and heterophilic interactions of Necl proteins in *SI Appendix*, Fig. S6.

Heterophilic and Homophilic Interactions of Necls Adhesive Specificity. The present study shows that the molecular basis of the interfacial area of the heterodimer of mNecl-4 Ig1 and mNecl-1 Ig1 (764.3 Å^2) is larger than that of the mNecl-1 Ig1 homodimer (708.8 Å^2). Previous studies have shown that Necl-1, Necl-2, and Necl-3 can self-dimerize through homophilic interactions whereas Necl-1/Necl-4 and Necl-2/Necl-3 form heterodimers via specific heterophilic interactions (43). Necl-4 interacts with Necl-1 to form a Schwann cell–axon interface (14, 15). Necl-2 and Necl-3 form a transsynaptic adhesion complex that increases the number of functional excitatory synapses (43). The strong heterophilic binding between different Necl proteins is probably enhanced by electrostatic interactions outside the hydrophobic interaction core. The structure of the mNecl-4 and mNecl-1 ectodomain heterodimer complex demonstrates that the interaction interface comprises a hydrophobic core and several charged residues that line up on the

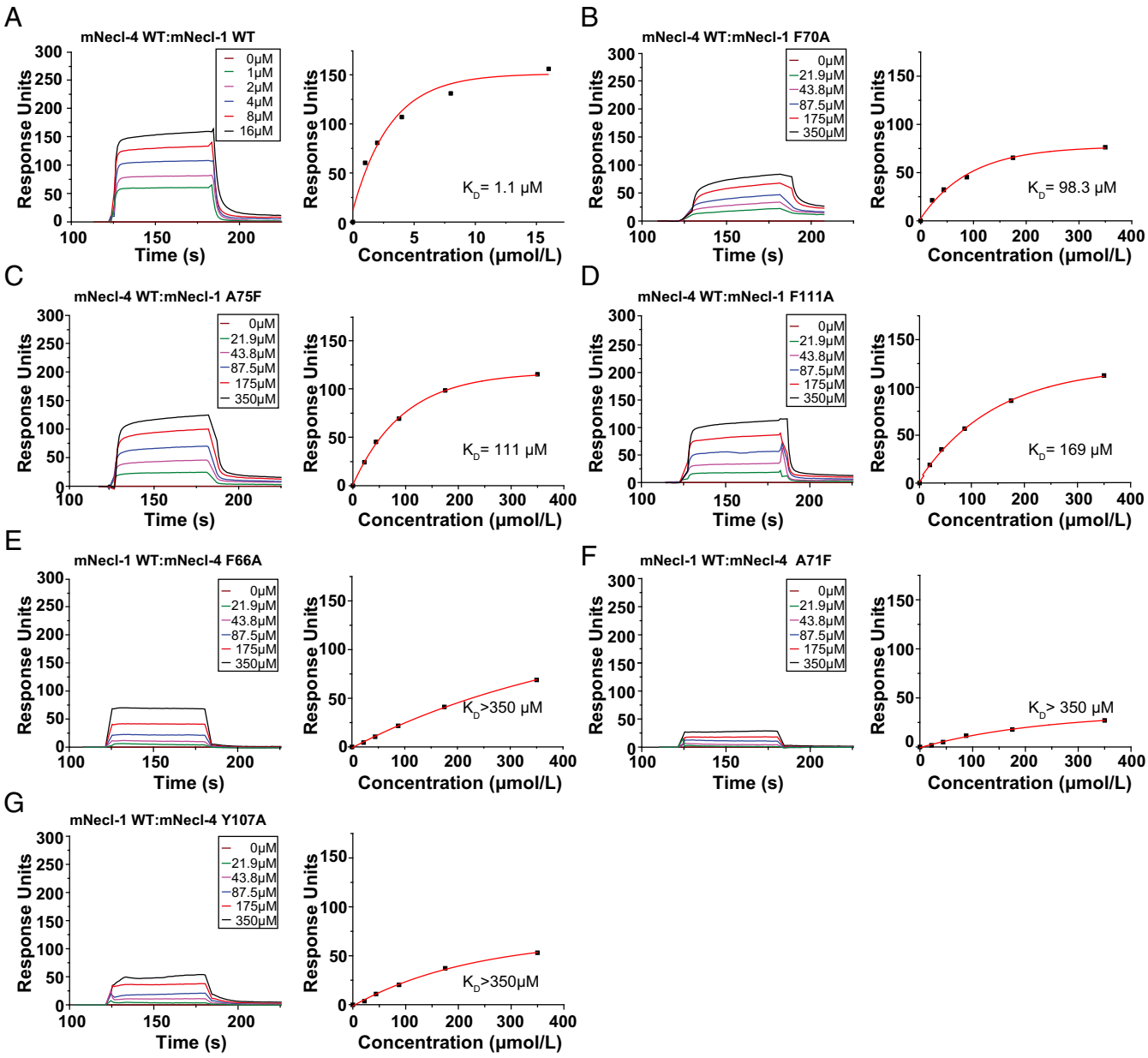

Fig. 4. Equilibrium dissociation constants of interactions between mNecl-4/mNecl-1 and their mutants. (*A*) The steady-state analysis revealed that the Ig1 domain of mNecl-1 WT binds the full ectodomain of mNecl-4 WT with a K_D value of ~1.1 μM. (*B–D*) The steady-state analysis revealed that the F70A, A75F, and F111A single mutants of mNecl-1 bind mNecl-4 WT with K_D values of ~98.3 μM, 111 μM, and 169 μM, respectively. (*E–G*) The steady-state analysis revealed that the F66A, A71F, and Y107A single mutants of mNecl-4 bind mNecl-1 WT with K_D values over 350 μM (the calculated K_D values were 926 μM, 400 μM, and 418 μM, respectively).

edge of the interface (Fig. 3). These residues form polar interactions with each other that serve to stabilize the heterophilic interaction. In particular, positively charged Arg77 of mNecl-1 forms salt bridges with negatively charged Asp50 and Glu109 of the mNecl-4 Ig1 domain. The distances between these salt bridges are 3.5 Å and 4.8 Å, respectively (*SI Appendix*, Fig. S6). Additionally, Gln66 of mNecl-1 accepts a hydrogen bond from His113 of mNecl4 (distance = 3.4 Å). Residues Arg77 and Gln66 are well conserved in the family, and Asp50, Glu109, and His113 are highly conserved in Necl-4 homologs (Fig. 1*C*). Compared with that of the heterophilic interaction between Necl-1 and Necl-4, the affinity of the homophilic interaction of Necl-1 or the heterophilic interaction between Necl-1 and Necl-2 is weaker (43), which may be due to the lack of polar contacts on the rim of the hydrophobic core of the interfacial area. Necl-2 and Necl-4, which both have charge compatibility residues on either side but cannot form intensive binding (43), are exceptions to this model, possibly due to N-linked glycans that hamper adhesion and destabilize the *trans* dimer. Hence, the polar contacts outside the buried hydrophobic surface areas may confer heterophilic and homophilic binding specificity to the Necl family (*SI Appendix*, Fig. S6).

Physiological Roles of the Heterophilic and Homophilic Interactions of Necl Family Proteins. Necl family members are widely expressed in many tissues, especially in the nervous system, and participate in selective homophilic or heterophilic interactions that contribute to cell–cell adhesion in developmental or pathological processes. Hence, strong competition exists between homophilic and heterophilic associations, and many Necls or IgCAMs are present at the surface of the membrane to mediate cell–cell adhesion. The results of this study suggest that the heterophilic interactions of

Table 3. SPR analysis of heterodimerization between mNecl-4 Ig1 to Ig3 and mNecl-1 Ig1

Proteins	K_D dimerization, μM
mNecl-4 WT with mNecl-1 WT	1.1
mNecl-4 WT with mNecl-1 mutants	
mNecl-4 WT with mNecl-1 Q66A	2.44
mNecl-4 WT with mNecl-1 V115A	3.73
mNecl-4 WT with mNecl-1 Q65A	6.01
mNecl-4 WT with mNecl-1 T67A	6.14
mNecl-4 WT with mNecl-1 M113A	17.7
mNecl-4 WT with mNecl-1 Q59A	19.8
mNecl-4 WT with mNecl-1 R77A	26.4
mNecl-4 WT with mNecl-1 L76A	31.1
mNecl-4 WT with mNecl-1 F70A	98.3
mNecl-4 WT with mNecl-1 A75F	111
mNecl-4 WT with mNecl-1 F111A	169
mNecl-4 WT with mNecl-1 F70A-F111A	ND
mNecl-1 WT with mNecl-4 mutants	
mNecl-1 WT with mNecl-4 Q62A	22.7
mNecl-1 WT with mNecl-4 N31Q N262Q N286Q	66.5
mNecl-1 WT with mNecl-4 F66A	>350
mNecl-1 WT with mNecl-4 A71F	>350
mNecl-1 WT with mNecl-4 Y107A	>350
mNecl-1 WT with mNecl-4 F66A-Y107A	>350

ND, not determined.

the Necl proteins have a higher affinity than the homophilic interactions. For example, the interfacial area between mNecl-4 Ig1 and mNecl-1 Ig1 is 764.3 Å^2, which is larger than that between monomers in the mNecl-1 Ig1 homodimer (708.8 Å^2) or the mNecl-3 Ig1 homodimer (698 Å^2), as shown by PDBePISA analysis.

During nervous system development, various types of neurons are first produced and then project their axons to establish functional circuitry. At this time, multiple bare axons are fasciculated as bundles along well-organized paths. Glial cells are generated during the subsequent gliogenic phase and are matched to axons to subsequently separate the axons and establish myelin sheaths around individual axons (49). The dynamic interactions between axons and oligodendrocytes or Schwann cells require the precise control of the expression of many different cell adhesion molecules. Necl-4 and Necl-1 mediate peripheral Schwann cell–axon interactions, and Necl-4 is expressed in myelinating Schwann cells and serves as a binding partner for Necl-1, which is localized to the contact sites between axons. Notably, the expression of Necl-4 in Schwann cells is up-regulated as myelination is initiated (14, 15). Therefore, as the premyelinating Schwann cells project lamellipodia-like processes into the axonal bundles, a Necl-4–Necl-1 heterophilic interaction may form and allow the Schwann cells to ensheathe and wrap the axons whereas the homophilic interaction between Necl-1 may be abolished, allowing the axon bundle to be individually segregated. Thus, the present study provides structural and biological insights into the transition from the homophilic interaction of Necl-1/Necl-1 to the heterophilic interaction of Necl-1/Necl-4 between axons and Schwann cells during the myelination process.

Methods

Protein Expression and Purification. The cDNA fragment encoding the extracellular regions (Ig1 to Ig3) of mouse Necl-4 (Glu25 to Ala317) and a C-terminal His6 tag were inserted between the BglII and XhoI sites of the Bac-to-Bac baculovirus expression system vector pFastBac1 (Invitrogen). The baculovirus hemolin signal sequence was used to facilitate the secretion of the protein. The point mutations N31Q, Q62A, F66A, A71F, Y107A, N262Q, and N286Q in mouse Necl-4 Ig1 to Ig3 and all other mutation combinations were introduced using a Fast Mutagenesis System (TransGen). The recombinant baculovirus was first amplified in Sf21 cells and then used to infect High Five cells to produce soluble Necl-4 protein. The secreted protein was collected from the medium by nickel-nitrilotriacetic acid (Ni-NTA) affinity chromatography and then purified by a Superdex 75 column (GE Healthcare). The purified protein was concentrated to 7 mg/mL in 150 mM NaCl and 20 mM Tris-Cl, pH 8.0.

The expression and purification of the Necl-1 Ig1 protein followed a published procedure (22). In brief, an N-terminal 6× His tag and the coding sequence of the mouse Necl-1 Ig1 domain (Asn23 to Ile133) were subcloned into the BamHI and XhoI sites of pET-32a and subsequently transformed into *E. coli* strain BL21 (DE3) for expression. The point mutations Q59A, Q65A, Q66A, T67A, F70A, A75F, L76A, R77A, F111A, M113A, and V115A in the mouse Necl-1 Ig1 domain and all other combinations were introduced using a Fast Mutagenesis System (TransGen). The protein was first purified with Ni-NTA resin, followed by a Superdex 200 column (GE Healthcare).

svAUC. Sedimentation velocity experiments were performed in a ProteomeLab XL-I analytical ultracentrifuge (Beckman Coulter) equipped with an AN-60Ti rotor (four-holes) and conventional double-sector aluminum centerpieces with a 12-mm optical path length. The mNecl-4 protein was diluted to 0.6 mg/mL, and mNecl-1 was diluted to 0.7 mg/mL; 380 μL of sample and 400 μL of buffer (20 mM Hepes, 150 mM NaCl, pH 8.0) were then loaded. After equilibration for ∼1 h at 20 °C, experiments were carried out at 52,000 rpm using continuous scan mode and a radial spacing of 0.003 cm. Data were collected at 3-min intervals at 280 nm. The fitting of absorbance versus cell radius data was performed using SEDFIT software (https://sedfitsedphat.nibib.nih.gov/software/default.aspx) and a continuous sedimentation coefficient distribution c(s) model, covering a range of 0 to 15 S. The buffer composition (density and viscosity) and protein partial specific volume (V-bar) were calculated using Sednterp.

His$_6$ Tag Pulldown Assays. The C-terminal 6× His-tagged mNecl-4 full ectodomain (Ig1 to Ig3) was preincubated with an mNecl-1 Ig1 domain whose His tag was removed by thrombin cleavage. In the mixture, the mNecl-4 ectodomain mixed with the mNecl-1 Ig1 domain at a molar ratio of 1:1. Then, the protein mixture was loaded onto an Ni-NTA column (Qiagen) and purified. The samples obtained from each step of the purification were analyzed by SDS/PAGE. To recover the protein that was tightly bound to the resin, the Ni-NTA beads were finally heated at 98 °C and dissolved in SDS/PAGE loading buffer.

SPR for Binding Studies. The binding affinity between mNecl-4 and mNecl-1 Ig1 was analyzed on a Biacore 3000 machine with CM5 chips (GE Healthcare) at room temperature (25 °C). For the SPR measurements, all proteins were purified by gel filtration using a Superdex 75 column (GE Healthcare) and diluted in Hepes buffer consisting of 20 mM Hepes (pH 7.5), 150 mM NaCl, and 0.005% (vol/vol) Tween-20. Necl-4 (WT) and Necl-1 Ig1 (WT) were diluted to 20 μg/mL and immobilized on a CM5 chip using a standard amine coupling method.

The analytes were diluted in running buffer to a series of concentrations and injected at 30 μL per min for 60 s, after which they were subjected to a 120-s dissociation phase. The binding signals returned to baseline after the dissociation phase finished. The binding affinity (K_D) was analyzed with BIAevaluation Version 4.1 using the 1:1 Langmuir binding model. These protein concentration ranges were obtained using a twofold dilution series. The analyses were performed in duplicate to increase the concentration. The collected data and the final statistics are summarized in Table 3.

Crystallization and Structure Determination. Crystals of the mouse Necl-4 ectodomain containing Ig1 to Ig3 were grown in a hanging drop vapor diffusion system at 18 °C. In total, 0.5 μL of the protein sample (7 mg/mL) was mixed with 0.5 μL of reservoir buffer before the crystallization trials. The final refined crystallization conditions were 0.04 M potassium dihydrogen phosphate, 10% (wt/vol) PEG 8000, and 25% glycerol. Since the glycerol present in the reservoir buffer could serve as a cryoprotectant, the crystals of mNecl-4 were directly frozen in liquid nitrogen. To crystallize the mNecl-1–mNecl-4 complex, the purified mNecl-1 Ig1 domain and mNecl-4 Ig1 to Ig3 domain were mixed at a 1:1 molar ratio and incubated at 4 °C overnight. The mixture was concentrated to 6 mg/mL and used for the crystallization trials in a sitting-drop vapor diffusion system. The final refined crystallization condition was 0.2 M calcium acetate, 0.1 M Hepes sodium salt, pH 7.5, and 10% (wt/vol) PEG 8000. The crystals were flash frozen in liquid nitrogen with 15% (vol/vol) ethylene glycol as a cryoprotectant.

The crystal of the mNecl-4 full ectodomain with the N31Q, N262Q, and N286Q mutations belonged to the space group I422 and contained one molecule per ASU. To solve the crystal structure, we used the native SAD method as previously described (44, 45). In brief, a low-dose multiorientation data collection strategy was used to obtain highly redundant diffraction data at macromolecular crystallography beamline X06DA (PXIII) at the Swiss Light Source. The X-ray energy was 6 keV (wavelength 2.077 Å), and the diffraction datasets were collected by a Pilatus 2M-F detector. Sixteen datasets were

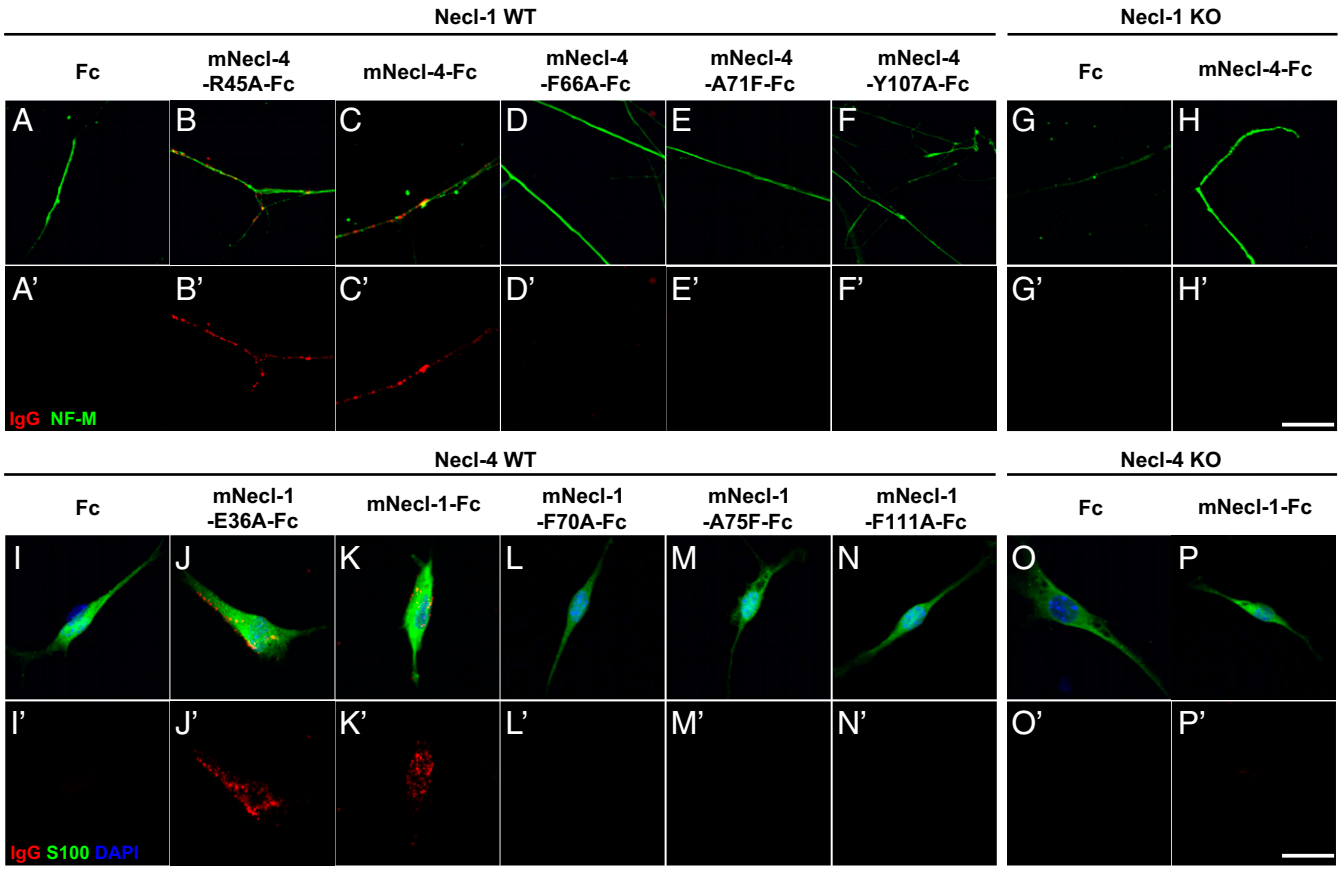

Fig. 5. Key residues mediated the heterophilic binding between the Necl-4 and Necl-1 ectodomains. (*A–F* and *A′–F′*) Different binding of WT and mutant mNecl-4-Fc fusion proteins to DRG neurons derived from Necl-1 WT mice. Binding of Fc fusion proteins was detected using a secondary antibody specific for hFc (red); neurites were labeled with an antibody specific for neurofilament M (NF-M, green). (*G*, *G′*, *H*, and *H′*) Binding of Fc and the mNecl-4-Fc fusion protein to DRG neurites derived from Necl-1 knockout (Necl-1 KO) mice. (*I–N* and *I′–N′*) Different binding of WT and mutant mNecl-4-Fc fusion proteins to Schwann cells derived from Necl-4 WT mice. Binding of Fc fusion proteins was detected using a secondary antibody specific for hFc (red), Schwann cells were labeled with an antibody specific for S100 (green), and DAPI was used to label the Schwann cell nucleus (blue). (O, O′, P, and P′) Binding of Fc and the mNecl-1-Fc fusion protein to Schwann cells derived from Necl-4 knockout (Necl-4 KO) mice. (Scale bar: 20 μm.)

collected from a single crystal at two different sites in eight different crystal orientations using a multiaxis goniometer (PRIGo). All diffraction data were indexed, integrated, and scaled using the XDS package (50, 51), and 14 datasets were merged using XSCALE. The data quality was assessed using PHENIX. XTRIAGE (52). The sulfur sites were identified using SHELXD (53) in 1,000 trials with a cutoff of 3.2 Å. The phasing of the structure was performed using SHELXE (53), which yielded an experimental phased map. The initial model of the mNecl-4 ectodomain was built with BUCCANEER (54), followed by manual model building with the COOT software (55). The final model of the mNecl-4 ectodomain was obtained by using a dataset collected with higher energy X-rays (1.0 Å), which reached a resolution of 2.2 Å. The structure was solved by performing molecular replacement using the initial model generated from the native SAD datasets. The crystal of the mNecl-4 ectodomain complex with the mNecl-1 Ig1 domain diffracted the X-rays to 3.3 Å. This crystal belonged to the P321 space group and contained two copies of the mNecl-4 ectodomain and one copy of the mNecl-1 Ig1 domain. To solve the crystal structure, the atomic models of the mNecl-4 ectodomain and the human Necl-1 Ig1 domain (PDB ID code 1Z9M) were used as the searching models for molecular replacement using Phaser for MR (56). While the search for the human Necl-1 Ig1 model found multiple solutions, the search for the mNecl-4 full ectodomain containing the Ig1 to Ig3 domains could not find a solution without clashes. We speculate that the following two difficulties occurred in the molecular replacement: (*i*) The Ig domains of mNecl-4 or mNecl-1 have similar folding overall, and (*ii*) due to the flexible linkage between the Ig domains, the relative position between adjacent Ig domains of mNecl-4 may vary in different crystal lattices; thus, the mNecl-4 full ectodomain might have a different conformation. To solve these problems, we truncated the full ectodomain of mNecl-4 into smaller fragments containing Ig1-Ig2 or Ig2-Ig3, and the search using these models yielded a single solution. Based on this solution, we finally located the Ig1 domain of mNecl-1 in the structure. The final model of the complex was obtained by manual model building using COOT; in particular, in the loop region between the F and G β-strands (F-and-G-loop) of the mNecl-4 Ig1 domain, significant conformational rearrangements occurred due to the involvement of these regions in the interaction with mNecl-1 Ig1. The data collection and refinement statistics are summarized in Table 1.

Animals and Primary Cell Culture. Necl-1 knockout mice, Necl-4 knockout mice, and WT mice were obtained as previously described (32, 57). All mice were housed on a 12-h light/dark cycle, and all efforts were made to minimize their suffering. All animal care and experiments were approved by the Institutional Animal Care and Use Committee of the Chinese Academy of Medical Sciences and Peking Union Medical College with all procedures in compliance with the Experimental Animal Regulations (China Science and Technology Commission Order No. 2).

DRG neurons were isolated from C57BL/6J mice at E14.5, and sciatic nerve Schwann cells were isolated from P3 mice as previously described (58, 59). After 3 wk of culture, the cells were used for Fc fusion protein binding experiments.

Fc Fusion Protein Binding Experiments. The binding experiments were carried out by incubating the cells with medium containing different Fc fusion proteins preincubated with anti-human Fc-Cy3 (The Jackson Laboratory), as previously described (14). The cDNA fragment encoding the signal peptide and extracellular region of mouse Necl-1 (bp 1 to 984 of the CDS region) was inserted between the HindIII and XbaI sites of pIg-plus. The cDNA fragment encoding the signal peptide and extracellular region of mouse Necl-4 (bp 1 to 951 of the CDS region) was inserted between the XhoI and XbaI sites. The mNecl-1 and mNecl-4 mutations were introduced using a Fast Mutagenesis System (TransGen). The Fc fusion proteins were expressed in the 293ET cell line and purified by a protein

A column (Thermo), and their concentrations were measured by a bicinchoninic acid (BCA) assay. For the binding experiments, conditioned media containing 0.4 μg of the various Fc fusion proteins were mixed with 0.3 μg of Cy3-conjugated anti-human Fc antibody for 60 min and incubated with the cells as indicated in each figure for 2 h at room temperature. The unbound protein was removed by three washes with PBS, and the cells were fixed with 4% paraformaldehyde (PFA). The axons of the DRG neurons were observed by anti-neurofilament-M (NF-M) staining (1:2,000, PCK-593P-100; Covance), and Schwann cells were observed by S100 staining (1:200, ab868; Abcam).

Data Availability. Coordinates and structural factors for the X-ray structures of mNecl-4 and the mNecl-4/mNecl-1 ectodomain complex are deposited in the Protein Data Bank, as PDB ID codes 5ZO1 and 5ZO2, respectively.

ACKNOWLEDGMENTS. We thank the Swiss Light Source X06DA beamline facility (Villigen, Switzerland) for beam time and assistance with native SAD data collection and structure determination. We thank the staff of the BL17B/BL18U1/BL19U1/BL19U2/BL01B beamlines at the National Center for Protein Science Shanghai and the Shanghai Synchrotron Radiation Facility (Shanghai, People's Republic of China) for assistance during data collection. We also thank Qian Wang (Institute of Microbiology, Chinese Academy of Sciences), who helped with the AUC experiment. This work was supported by National Key Research and Development Program of China Grants 2016YFA0100702 and 2016YFC0902502; National Natural Science Foundation of China Grants 31670789 and 31671316; and Chinese Academy of Medical Sciences (CAMS) Innovation Fund for Medical Sciences (CIFMS) Grants 2016-I2M-2-001, 2016-I2M-1-001, 2016-I2M-1-004, 2017-I2M-2-004, 2017-I2M-3-010, and 2017-I2M-1-004.

1. Chothia C, Gelfand I, Kister A (1998) Structural determinants in the sequences of immunoglobulin variable domain. *J Mol Biol* 278:457–479.
2. Leshchyns'ka I, Sytnyk V (2016) Reciprocal interactions between cell adhesion molecules of the immunoglobulin superfamily and the cytoskeleton in neurons. *Front Cell Dev Biol* 4:9.
3. Biederer T (2006) Bioinformatic characterization of the SynCAM family of immunoglobulin-like domain-containing adhesion molecules. *Genomics* 87:139–150.
4. Takai Y, Ikeda W, Ogita H, Rikitake Y (2008) The immunoglobulin-like cell adhesion molecule nectin and its associated protein afadin. *Annu Rev Cell Dev Biol* 24:309–342.
5. Takai Y, Nakanishi H (2003) Nectin and afadin: Novel organizers of intercellular junctions. *J Cell Sci* 116:17–27.
6. Takai Y, Irie K, Shimizu K, Sakisaka T, Ikeda W (2003) Nectins and nectin-like molecules: Roles in cell adhesion, migration, and polarization. *Cancer Sci* 94:655–667.
7. Takahashi K, et al. (1999) Nectin/PRR: An immunoglobulin-like cell adhesion molecule recruited to cadherin-based adherens junctions through interaction with Afadin, a PDZ domain-containing protein. *J Cell Biol* 145:539–549.
8. Rubinstein R, Ramagopal UA, Nathenson SG, Almo SC, Fiser A (2013) Functional classification of immune regulatory proteins. *Structure* 21:766–776.
9. Ikeda W, et al. (2003) Tage4/Nectin-like molecule-5 heterophilically trans-interacts with cell adhesion molecule Nectin-3 and enhances cell migration. *J Biol Chem* 278:28167–28172.
10. Kakunaga S, et al. (2005) Nectin-like molecule-1/TSLL1/SynCAM3: A neural tissue-specific immunoglobulin-like cell-cell adhesion molecule localizing at non-junctional contact sites of presynaptic nerve terminals, axons and glia cell processes. *J Cell Sci* 118:1267–1277.
11. Williams YN, et al. (2006) Cell adhesion and prostate tumor-suppressor activity of TSLL2/IGSF4C, an immunoglobulin superfamily molecule homologous to TSLC1/IGSF4. *Oncogene* 25:1446–1453.
12. Pellissier F, Gerber A, Bauer C, Ballivet M, Ossipow V (2007) The adhesion molecule Necl-3/SynCAM-2 localizes to myelinated axons, binds to oligodendrocytes and promotes cell adhesion. *BMC Neurosci* 8:90.
13. Niederkofler V, Baeriswyl T, Ott R, Stoeckli ET (2010) Nectin-like molecules/SynCAMs are required for post-crossing commissural axon guidance. *Development* 137:427–435.
14. Spiegel I, et al. (2007) A central role for Necl4 (SynCAM4) in Schwann cell-axon interaction and myelination. *Nat Neurosci* 10:861–869.
15. Maurel P, et al. (2007) Nectin-like proteins mediate axon Schwann cell interactions along the internode and are essential for myelination. *J Cell Biol* 178:861–874.
16. Zinn K, Özkan E (2017) Neural immunoglobulin superfamily interaction networks. *Curr Opin Neurobiol* 45:99–105.
17. Mandai K, Rikitake Y, Mori M, Takai Y (2015) Nectins and nectin-like molecules in development and disease. *Curr Top Dev Biol* 112:197–231.
18. Samanta D, et al. (2012) Structure of Nectin-2 reveals determinants of homophilic and heterophilic interactions that control cell-cell adhesion. *Proc Natl Acad Sci USA* 109:14836–14840.
19. Harrison OJ, et al. (2012) Nectin ectodomain structures reveal a canonical adhesive interface. *Nat Struct Mol Biol* 19:906–915.
20. Narita H, et al. (2011) Crystal structure of the cis-dimer of nectin-1: Implications for the architecture of cell-cell junctions. *J Biol Chem* 286:12659–12669.
21. Fogel AI, et al. (2010) N-glycosylation at the SynCAM (synaptic cell adhesion molecule) immunoglobulin interface modulates synaptic adhesion. *J Biol Chem* 285:34864–34874.
22. Dong X, et al. (2006) Crystal structure of the V domain of human nectin-like molecule-1/Syncam3/Tsll1/Igsf4b, a neural tissue-specific immunoglobulin-like cell-cell adhesion molecule. *J Biol Chem* 281:10610–10617.
23. Samanta D, Guo H, Rubinstein R, Ramagopal UA, Almo SC (2017) Structural, mutational and biophysical studies reveal a canonical mode of molecular recognition between immune receptor TIGIT and nectin-2. *Mol Immunol* 81:151–159.
24. Deuss FA, Gully BS, Rossjohn J, Berry R (2017) Recognition of nectin-2 by the natural killer cell receptor T cell immunoglobulin and ITIM domain (TIGIT). *J Biol Chem* 292:11413–11422.
25. Zhang S, et al. (2013) Competition of cell adhesion and immune recognition: Insights into the interaction between CRTAM and nectin-like 2. *Structure* 21:1430–1439.
26. Zhang X, et al. (2013) Structure of measles virus hemagglutinin bound to its epithelial receptor nectin-4. *Nat Struct Mol Biol* 20:67–72.
27. Zhang N, et al. (2011) Binding of herpes simplex virus glycoprotein D to nectin-1 exploits host cell adhesion. *Nat Commun* 2:577.
28. Di Giovine P, et al. (2011) Structure of herpes simplex virus glycoprotein D bound to the human receptor nectin-1. *PLoS Pathog* 7:e1002277.
29. Zhang P, et al. (2008) Crystal structure of CD155 and electron microscopic studies of its complexes with polioviruses. *Proc Natl Acad Sci USA* 105:18284–18289.
30. Sara Y, et al. (2005) Selective capability of SynCAM and neuroligin for functional synapse assembly. *J Neurosci* 25:260–270.
31. Biederer T, et al. (2002) SynCAM, a synaptic adhesion molecule that drives synapse assembly. *Science* 297:1525–1531.
32. Park J, et al. (2008) Disruption of nectin-like 1 cell adhesion molecule leads to delayed axonal myelination in the CNS. *J Neurosci* 28:12815–12819.
33. Yang H, Wittnam JL, Zubarev RA, Bayer TA (2013) Shotgun brain proteomics reveals early molecular signature in presymptomatic mouse model of Alzheimer's disease. *J Alzheimers Dis* 37:297–308.
34. Casey JP, et al. (2012) A novel approach of homozygous haplotype sharing identifies candidate genes in autism spectrum disorder. *Hum Genet* 131:565–579.
35. Takayanagi Y, et al. (2010) Impairment of social and emotional behaviors in Cadm1-knockout mice. *Biochem Biophys Res Commun* 396:703–708.
36. Zhiling Y, et al. (2008) Mutations in the gene encoding CADM1 are associated with autism spectrum disorder. *Biochem Biophys Res Commun* 377:926–929.
37. Albayrak Ö, et al.; Psychiatric GWAS Consortium: ADHD Subgroup (2013) Common obesity risk alleles in childhood attention-deficit/hyperactivity disorder. *Am J Med Genet B Neuropsychiatr Genet* 162B:295–305.
38. Sandau US, Alderman Z, Corfas G, Ojeda SR, Raber J (2012) Astrocyte-specific disruption of SynCAM1 signaling results in ADHD-like behavioral manifestations. *PLoS One* 7:e36424.
39. Raveh S, Gavert N, Spiegel I, Ben-Ze'ev A (2009) The cell adhesion nectin-like molecules (Necl) 1 and 4 suppress the growth and tumorigenic ability of colon cancer cells. *J Cell Biochem* 108:326–336.
40. Gao J, et al. (2009) Loss of NECL1, a novel tumor suppressor, can be restored in glioma by HDAC inhibitor-Trichostatin A through Sp1 binding site. *Glia* 57:989–999.
41. Kuramochi M, et al. (2001) TSLC1 is a tumor-suppressor gene in human non-small-cell lung cancer. *Nat Genet* 27:427–430.
42. Golan N, et al. (2013) Genetic deletion of Cadm4 results in myelin abnormalities resembling Charcot-Marie-Tooth neuropathy. *J Neurosci* 33:10950–10961.
43. Fogel AI, et al. (2007) SynCAMs organize synapses through heterophilic adhesion. *J Neurosci* 27:12516–12530.
44. Weinert T, et al. (2015) Fast native-SAD phasing for routine macromolecular structure determination. *Nat Methods* 12:131–133.
45. Olieric V, et al. (2016) Data-collection strategy for challenging native SAD phasing. *Acta Crystallogr D Struct Biol* 72:421–429.
46. Waltersperger S, et al. (2015) PRIGo: A new multi-axis goniometer for macromolecular crystallography. *J Synchrotron Radiat* 22:895–900.
47. Einheber S, Milner TA, Giancotti F, Salzer JL (1993) Axonal regulation of Schwann cell integrin expression suggests a role for alpha 6 beta 4 in myelination. *J Cell Biol* 123:1223–1236.
48. Eshed Y, et al. (2005) Gliomedin mediates Schwann cell-axon interaction and the molecular assembly of the nodes of Ranvier. *Neuron* 47:215–229.
49. Nave KA, Werner HB (2014) Myelination of the nervous system: Mechanisms and functions. *Annu Rev Cell Dev Biol* 30:503–533.
50. Kabsch W (2010) Integration, scaling, space-group assignment and post-refinement. *Acta Crystallogr D Biol Crystallogr* 66:133–144.
51. Kabsch W (2010) Xds. *Acta Crystallogr D Biol Crystallogr* 66:125–132.
52. Adams PD, et al. (2010) PHENIX: A comprehensive Python-based system for macromolecular structure solution. *Acta Crystallogr D Biol Crystallogr* 66:213–221.
53. Sheldrick GM (2010) Experimental phasing with SHELXC/D/E: Combining chain tracing with density modification. *Acta Crystallogr D Biol Crystallogr* 66:479–485.
54. Cowtan K (2006) The Buccaneer software for automated model building. 1. Tracing protein chains. *Acta Crystallogr D Biol Crystallogr* 62:1002–1011.
55. Emsley P, Cowtan K (2004) Coot: Model-building tools for molecular graphics. *Acta Crystallogr D Biol Crystallogr* 60:2126–2132.
56. McCoy AJ (2007) Solving structures of protein complexes by molecular replacement with Phaser. *Acta Crystallogr D Biol Crystallogr* 63:32–41.
57. Zhu Y, et al. (2013) Necl-4/SynCAM-4 is expressed in myelinating oligodendrocytes but not required for axonal myelination. *PLoS One* 8:e64264.
58. Sleigh JN, Weir GA, Schiavo G (2016) A simple, step-by-step dissection protocol for the rapid isolation of mouse dorsal root ganglia. *BMC Res Notes* 9:82.
59. Honkanen H, et al. (2007) Isolation, purification and expansion of myelination-competent, neonatal mouse Schwann cells. *Eur J Neurosci* 26:953–964.